Plastic deformations of ceria nanocubes under compression: An atomistic simulations study

Gaétan Laurens, Jonathan Amodeo, Tristan Albaret

This article was originally published in Materialia in 2023. Please cite as:

G. Laurens, J. Amodeo, T. Albaret, Plastic deformations of ceria nanocubes under compression: An atomistic simulations study, Materialia. 30 (2023) 101824. https://doi.org/10.1016/j.mtla.2023.101824.

Plastic deformations of ceria nanocubes under compression : an atomistic simulations study

Gaétan Laurens[a], Jonathan Amodeo[b,c], Tristan Albaret,[a,*]

[a] *Institut Lumière Matière, UMR5306 Université Claude Bernard Lyon 1-CNRS, Université de Lyon, Villeurbanne 69622, France*
[b] *Université de Lyon, CNRS, INSA Lyon, UCBL, MATEIS, UMR5510, Villeurbanne 69621, France*
[c] *Aix-Marseille Université, Université de Toulon, CNRS, IM2NP, Marseille 13013, France*

Abstract

The mechanical properties and elementary deformation processes of ceria nanoparticles are investigated under uniaxial compression using quasi-static atomistic simulations and a fixed charge empirical potential. Results show a strong size-dependence of both the stress response and the plastic deformation phenomena that are characterized by amorphization and recrystallization processes that initiate from the surfaces in smaller-size samples, while the the propagation of {111} nanotwins is observed in larger nanoparticles. In particular, we point out that the recrystallized phase is made of reoriented fluorite that behaves as a structural seed for the nucleation of $\frac{1}{6}$ <112> {111} partial dislocations at the origin of the nanotwins. Similarities with plastic deformation processes of FCC metals at the nanoscale are outlined and discussed.

Keywords: Nanoparticles, Cerium Oxide, Plasticity, Mechanical deformation, MD Simulations

1. Introduction

Ceria (CeO_2) and its derivatives such as reduced ceria, doped ceria, ceria-based composites are currently employed in various domains of applications among which reactive chemistry, energy materials and medicine [1, 2]. Most of nanoceria applications are related to its catalytic properties [3] involved in hydrocarbon conversion reactions [4], three way catalysts [5], and water splitting reactions [6]. Regarding energy applications, cerium oxide is used in supercapacitors [7], batteries [8], solid oxide fuel cells [9] and solar cells [10]. More recently, ceria attracted a renewed interest in the field of biomedicine [11], as for instance in enzyme-mimetic chemistry [12], as well as for cancer [13] and neurological therapeutics [14]. Most of these applications rely on the redox properties of CeO_2-based nanomaterials that can easily be reduced to produce Ce^{3+} ions and oxygen vacancies. Several parameters regulate the Ce^{3+}/Ce^{4+} ratio and redox reactions. Among these, the surface over volume ratio (particularly high at the nanoscale) and the surface orientations are of primary importance [15, 16]. The most reactive surface of nanoceria is {100}, it is also the less stable when compared to {110} and {111} [16, 17, 18, 19]. The chemical composition of the environment and alloying elements as well impact the oxygen vacancy concentration in ceria and its chemical reactivity [20, 21, 22, 23]. Interestingly, several studies evidence the influence of strain on the oxygen transport and chemical reactivity [21, 22, 23]. In particular, grain boundaries have been shown to hamper the oxygen diffusion [22, 23]. Despite these applications, the mechanical properties of ceria nanocrystals have been scarcely characterized.

The mechanical properties of nanocrystals generally show a strong dependence on size and shape and raised a renewed interest since the early 2000' and the work of Uchic *et al.* [24, 25, 26, 27]. Essentially, the main characteristics of nano-objects mechanical properties when compared to bulk can be summarized as follows: (i) they typically show an extended elastic limit; (ii) dissipation mechanisms are often triggered by a dislocation nucleation process (instead of the classical multiplication one); (iii) plastic deformation tends to occur at particularly high

*Corresponding author

stress (in the GPa range) due to the lack of pre-existing defects. The characterization of plastic deformation elementary processes in nano-objects is quite demanding from an atomistic modelling point of view, and often require system sizes of at least several thousands of atoms which limits the applicability of electronic structure methods. To reach a sufficiently large system size in ceria, Sayle and coworkers employed dedicated empirical interatomic potentials to study the effect of large strains on ceria nanoparticles and nanowires. Mechanical properties of ceria nano-objects were investigated under compression [28, 29, 30] and tension [29, 31], some effects due to the nanoparticle shape were also discussed [28]. Several elementary processes responsible for plastic dissipation in ceria nanocrystals were identified including amorphization under compression in cuboidal, polyhedral and core-shell particles [28, 30], surface dislocation nucleation in compressed ⟨110⟩-oriented nanorods [29], and fluorite-to-rutile phase transformation in ⟨110⟩-oriented nanorods under tension [31]. Park *et al.* reported another phase transformation mechanism from the fluorite structure to a tetragonal phase occurring during the nanoindentation of CeO_2 thin films [32].

In the present paper, we perform nanocompression simulations of CeO_2 nanocubes with size ranging from 3 to 22 nm to investigate the elementary processes responsible for ceria deformation at the nanoscale. As the size increases, successive plastic dissipation mechanisms are identified while the yield stress increases. Among these mechanisms, a recrystallization process (local fluorite subgrain reorientation) is evidenced and discussed. The observed size dependent plastic behavior is rationalized and compared with observations made in other oxide and metal nanosystems.

2. Computational methods

2.1. Material properties calculations

Atomistic simulations in CeO_2 are performed using the open-source code LAMMPS [33] with the Born model parameterization of Sayle *et al.* [29] which was successfully employed in numerous nanomechanical studies [28, 29, 30, 34]. Charge summation is performed using the Multilevel Summation Method (MSM) with an accuracy on relative forces of 10^{-4} to efficiently assess the electrostatic interactions [35]. Structural energy minimizations were handled using either the conjugate gradient or the FIRE algorithms [36] until all atomic force components were found below a stopping criterion f_m=10^{-6}eV/Å.

To further validate the use of atomic interaction potentials, parts of the properties are also computed with DFT calculations using the VASP software [37, 38] with the projected augmented wave method (PAW) [39]. The DFT+U approach is employed to take into account strongly correlated and localized $4f$ electrons of Ce. A Hubbard U term is added to the LDA functional [40] (LDA+U) within the simplified rotationally invariant approach, introduced by Dudarev *et al.* [41]. The effective Hubbard term U_{eff} ($U_{eff} = U - J$) is chosen to be 5.3 eV. To model the fluorite bulk structure , we use a unit cell of 12 atoms with a Monkhorst-Pack mesh of $4 \times 4 \times 4$, as well as a cutoff energy of 500 eV for the Kohn-Sham wavefunctions. Geometry optimisations done with DFT are stopped whenever all the ionic force components are brought below a 10^{-3} eV/Å convergence criterion. Lattice and elastic properties computed for bulk ceria using the Sayle potential as well as DFT+U are presented in Table 1.

Table 1: Lattice and elastic properties of bulk CeO_2 computed using the Sayle [29] and DFT+U-PAW potentials. a is the lattice parameter in Å. C_{ij} are the components of the elastic constants tensor in GPa. The bulk modulus B, the shear modulus G, the Young's moduli E (in GPa) and the Poisson ratio ν are calculated using the Voigt approximation. E is the average Young modulus, $E_{[hkl]}$ provides the Young moduli in the $[hkl]$ direction.

Properties	Exp. [42]	DFT	Sayle
a	5.411	5.393	5.423
C_{11}	403	386.7	513.8
C_{12}	105	126.6	139.7
C_{44}	60	71.6	138.3
B	204.3	213.8	264.4
G	95.6	95.3	157.8
ν	0.297	0.306	0.251
E	248.1	248.8	394.8
$E_{[001]}$	359.6	324.4	454.1
$E_{[110]}$	189.8	215.8	374.1
$E_{[111]}$	164.0	193.9	353.3

In addition to lattice and elastic properties, Generalized Stacking Fault Energies (GSFE) [43] are also computed using the Sayle potential [29] to help at interpreting nanocompression outcomes. GSFE

inform on the stability and energy cost of various stacking faults providing valuable piece of information to dislocation models [44, 45]. GSFE calculation basically consists in computing the excess energy generated when shifting the atoms contained in the half-part of a columnar supercell along a single direction within the stacking fault plane (*e.g.,* along a Burgers vector direction) or mapping the entire plane, what leads to γ-line or γ-surface energy plots, respectively. Here, constrained GSFE are computed following the methodology employed by Guénolé *et al.* [46]. Starting from a $1 \times 1 \times 10$ supercell, the cell is reduced in the z direction perpendicular to the stacking fault plane, using a compressive strain ranging from 0 to 30% with strain steps of 5%. Practically, the upper-half part of the atoms is iteratively shifted along the x- and/or y-axis directions (in-plane directions) by a translation vector $\vec{t}$ while the third direction is tilted respect to z-axis by the same vector to preserve the simulation cell periodicity.

The energy of the system is minimized after each displacement down to a force norm of f_m=10^{-6}eV/Å. During each minimization, atoms are allowed to relax only perpendicularly to the fault plane (*i.e.,* along the z-axis) whereas the simulation box is kept unchanged to maintain the imposed strain condition.

2.2. Nanocompression simulation method

$\langle 100 \rangle$-oriented CeO_2 nanocubes with edge length of 3, 6, 11, 16 and 22 nm are built replicating the ceria unit cell in the 3 dimensions of space. Due to the polar nature of the $\{001\}$ fluorite surfaces (type 3 surface following the Tasker classification [47]), the *in silico* fabrication of CeO_2 nanocubes leads to hetero-surfaces *i.e.,* each $\langle 100 \rangle$ surface is entirely made up of cerium or oxygen atoms leading to charged surfaces. In order to avoid high energy and large forces in the initial configuration, [47, 48], half of the oxygen atoms from the O-rich surfaces are displaced to the opposite Ce-rich ones. This transformation reduces by a factor of two the surface effective charge as expected by charge redistribution mechanisms that allow the energetic stabilization of polar oxide surfaces [48]. After building, samples are relaxed using a force norm criterion of f_m=10^{-6} eV/Å.

Compression simulations are carried out using the quasi-static method where successive configurations are obtained after a deformation followed by the minimization of the potential energy [49]. To model the compression, two infinite and planar force fields representing the nanoindenter and the substrate are initially set at the top and bottom surfaces of the sample following the approach introduced by Issa and collaborators [50]. Each force field is defined as a repulsive harmonic potential with its normal aligned along the compression axis and a spring constant $K = 100$ eV/Å. During compression, the indenter is iteratively displaced along z, the compression axis direction, with a stepwise displacement corresponding to an engineering strain increment of $\Delta\varepsilon_{zz}$=-0.1 %. The zero strain state reference is fixed at the onset of contact homogeneity between the surfaces of the nanocube and the indenters. This state is usually preceded by a transient accomodation stage characterized by a partial contact. The axis of compression z is fixed and intially coincides with the [001] direction of the nanocrystal. In the following we only consider nanocubes under compression, for simplicity we will denote by "strain" the compressive strain using the notation $\varepsilon = -\varepsilon_{zz}$ to track the compressive strain as a positive quantity. After each indenter step the potential energy of the nanocube is minimized using a stopping criterion f_m=10^{-6}eVÅ, the both indenter force fields being kept fixed. The true compressive stress, $\sigma = f/S$, is calculated at each step using the instant indenter force f and contact area S, assuming a rectangular shape for the latter. σ is then estimated as the average between top and bottom surfaces. Atomic configurations are visualized using OVITO [51] and local crystal structures are identified using the Common Neighbor Analysis (CNA) algorithm [52] applied to the FCC Ce sublattice only.

3. Results

3.1. Mechanical response of CeO_2 nanocubes under compression

Stress-strain curves inferred from compression simulations of CeO_2 nanocubes are displayed in Figure 1(a). The data are reported after an accommodation stage during which pending atoms reorganize under the indenter which may lead to a non-zero initial stress observable in the figure at the lowest sizes. From this initial reference, all the curves display a nearly-linear regime consistent with a dominant elastic behaviour. At larger strain, a highly non-linear plastic deformation regime is obtained. During the first stages of compression

(ε <5%), small atomic rearrangements are observed in the vicinity of the surfaces, close to the indenters and substrate. These rearrangements evolve into disordered surface regions (see Figure 2(a.1)-(b.1)), in agreement with the high mobility of ceria ions of {001} polar surfaces [53]. For the larger nanocubes in the 11-22 nm size range, these regions are rather thin (∼5.5Å) *i.e.,* two times the interplanar distance between cerium layers in the <001> direction. Thicker disordered regions that expand up to ∼7.75-11Å (*i.e.* 3 to 4 {001} cerium layers) are generated in the smaller nanocubes (3 and 6 nm).

The onset of plastic deformation occurs at almost same strain whatever the system size, namely at 8 % ± 0.5 %, but at different yield stress. Indeed, the strength of ceria nanocubes decreases with size (*smaller is softer*) as shown by the comparative evolution of the [001] Young's modulus and the yield stress with respect to the size shown in Figure 1(b). This strength behaviour contradicts recent conclusions drawn from similar MD compression simulations performed in Si or Ni_3Al nanocubes for which the authors emphasize the lack of size-effect on the sample strength [27, 54, 55]. Indeed, the stress distribution in cubic-shaped sample is quasi-homogeneous what normally impedes size-effect if one assumes a unique deformation mechanism. However in ceria nanocubes, we will see that the size-effect can be attributed to changes in the elementary deformation processes rather than on size/shape-dependent stress concentration, as commonly observed in (non-cubic shaped) nanoparticles. For the smallest samples and up to 11 nm, the stress-strain curves show successive stress drops and reloads consecutive to the yield point followed by a steady-state regime at lower stress starting at about ε ∼17%. For larger sizes (16 and 22 nm), the initial plastic regime consists in a low-amplitude stress drop followed by a stress increase (strain-hardening) up to ε ∼12% where a large-amplitude stress drop happens, the rest of the stress-strain curves being characterized by a reload and similar steady-state regimes than in smaller-size nanoparticles.

3.2. Size-dependent elementary deformation processes of CeO_2 nanocubes

3.2.1. Sub-10 nm size nanocubes

The first significant stress drops observed between 8% and 10% strain in Figure 1(a) for the 3-nm and 6-nm samples are characterized by local amorphization starting from the surface. The

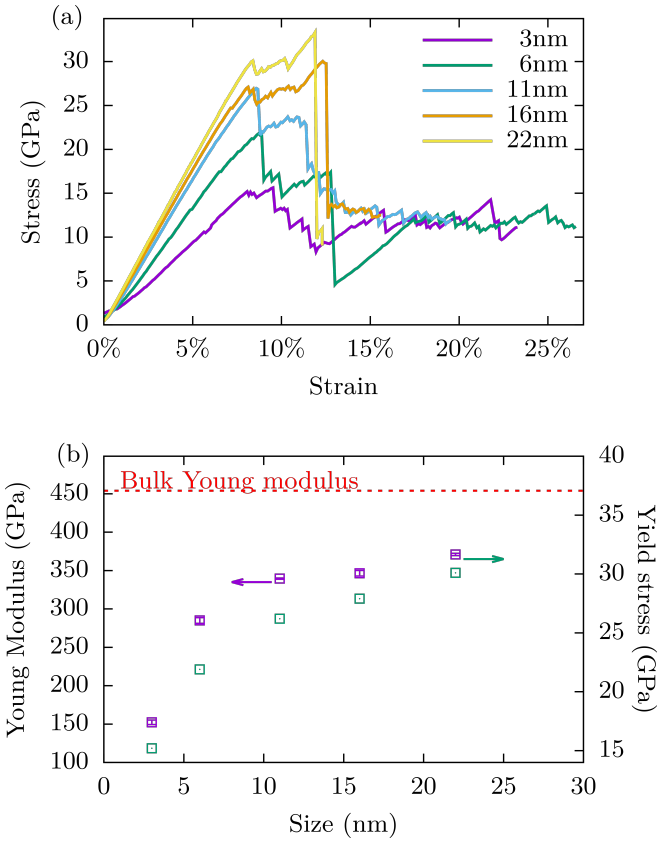

Figure 1: Mechanical response of ceria nanocubes under compression using MD. (a) Stress-strain curves, (b) Young's modulus (purple symbols) and yield stress (green symbols) with respect to the nanocube size. The yield stress is defined as the maximum stress along the stress-strain curve.

associated local plastic rearrangements are mostly made of bond-breaking and rebonding events, with a net production of under-coordinated 6-fold and 7-fold cerium atoms, compared to the 8-fold coordinated cerium in bulk fluorite (see details in Figure 3). During the larger stress drops, more intense structural rearrangements are located at the edges and corners of top and bottom surfaces where extruded beads are produced (Figure 2(a.2) and Figure 2(a.3)). Concurrently with the formation of the largest beads, the sample disorients as shown in Figure 2(a.3) where (010) atomic planes tilt out from their original orientation (the z compression axis). The presence of a tilt angle represents an additional route for stress dissipation.

Indeed, ⟨001⟩ is the strongest direction in ceria (see $E_{[hkl]}$ in Table 1), and any deviation from the compression axis induces softening. The maximum stress reduction σ_{tilt}^{max}, due to homogeneous sam-

ple reorientation can roughly be estimated from anisotropic elasticity:

$$\sigma_{tilt}(\theta, \varepsilon) = (E_{[001]} - \overline{E(\theta)})\varepsilon, \quad (1)$$

where θ is the tilt angle, ε is the engineering compressive strain imposed during the simulation and $\overline{E(\theta)}$ is the azimuthal average of the Young's modulus over the directions showing a θ tilt angle with respect to [001]. $\overline{E(\theta)}$ is calculated using the anisotropic elasticity in a cubic crystal (see [56] for an example in diamond silicon). Using Equation 1, the crystal reorientation contribution to stress is moderate up to ε =10% strain with a stress reduction of 0.2 GPa in the 3-nm and 6-nm cubes for a tilt angle of $\sim 4.3°$. It increases at 20 % strain up to 2.7 GPa and 5.9 GPa for the 3-nm and 6-nm samples and tilt angles of $\sim 11.1°$ and $\sim 17.2°$, respectively.

In summary, the dominant plastic mechanism of sub-10 nm size ceria nanocubes relies on an amorphization process starting from the surfaces. Nonetheless, this process can be associated with crystal reorientation with respect to the compressive axis that enhances the plastic deformation process.

3.2.2. Intermediate size nanocubes

Initially, the plastic behavior of the 11-nm edge nanocubes compares with smaller samples: from 8 % of strain, amorphous regions appear on the opposite top and bottom edges/corners of the nanocubes what leads to the reorientation of the rest of the sample.

At slightly larger strain ($\varepsilon \gtrsim 12\%$), phase transformation occurs in pyramidal-shape domains which appear as triangular regions in Figure 2(b.3) after a 2D projection in the (100) plane.

Further crystallographic analysis show that the local atomic arrangement in the transformed region still correspond to the fluorite structure but with a different orientation as in a recrystallization process. Considering the original frame $\{[\bar{1}10],[\bar{1}\bar{1}0],[001]\}$ shown before transformation in Figure 4(a), the recrystallized fluorite structure has a $\{[001],[\bar{1}10],[\bar{1}\bar{1}0]\}$ orientation (Figure 4(b)). During the transformation, the network of Ce atoms follows a smooth and continuous evolution driven by the compression which is comparable to the FCC-to-BCC Bain transformation observed in metals [57]. However, the transformation observed in CeO_2 involves the disruption and creation of Ce-O bonds that make the transformation irreversible. Both configurations can easily be recognized using plane projections. As seen in Figure 4, the Ce 2D-units of the original structure initially draw a left-oriented parallelogram while the transformed Ce 2D-units are arranged as squares using the same projection.

Before examining further the recrystallization process, we verified whether the observed plastic process is a bias of the Sayle interaction potential or if it can be validated by a more accurate electronic structure model. To do so, we performed Nudged Elastic Band (NEB) calculations [58] with the climbing technique [59] using DFT (VASP code) and the Sayle's potential on the same CeO_2 fluorite unit cell containing 6 atoms. The NEB calculations are designed with the starting point as the original fluorite unit cell (as oriented before recrystallization) and the ending point as the recrystallized configuration. The cell parameters of the intermediate images are fixed as a linear interpolation between these two limits, 11 images are built for the VASP and classical calculations. We checked that increasing the number of images to 101 images in the NEB classical calculation changes the energy barriers by less than 0.1 meV per crystal unit. The only variational parameters are the positions of the atoms for each image. A spring constant of 1 eV/Å^2 is used between the atoms of neighbouring images along the NEB path and the convergence criterion on the atomic forces is set to 5×10^{-3} eV/Å.

To mimic the compression simulation, the starting NEB configuration is deformed to ε=15% and ε=30%. Simulation results are provided in Figure 5. Activation energy barriers computed using DFT and the Sayle potential are reasonably comparable up to ε=15% strain, which is above the critical strain for triggering recrystallization in the quasi-static compression simulation. Both DFT and Sayle potential NEB simulations show that increasing strain in the original fluorite structure is favourable to the recrystallization process reducing the activation energy barrier. From a configurational point of view, the two models show similar configurations with 6-fold coordinated cerium atoms at the saddle point (Figure 5, top panel). While an approach including Grain Boundary (GB) formation energy would help at providing a more comprehensive description of the recrystallization process in nanoceria, here we confirm the capability of the Sayle inter-

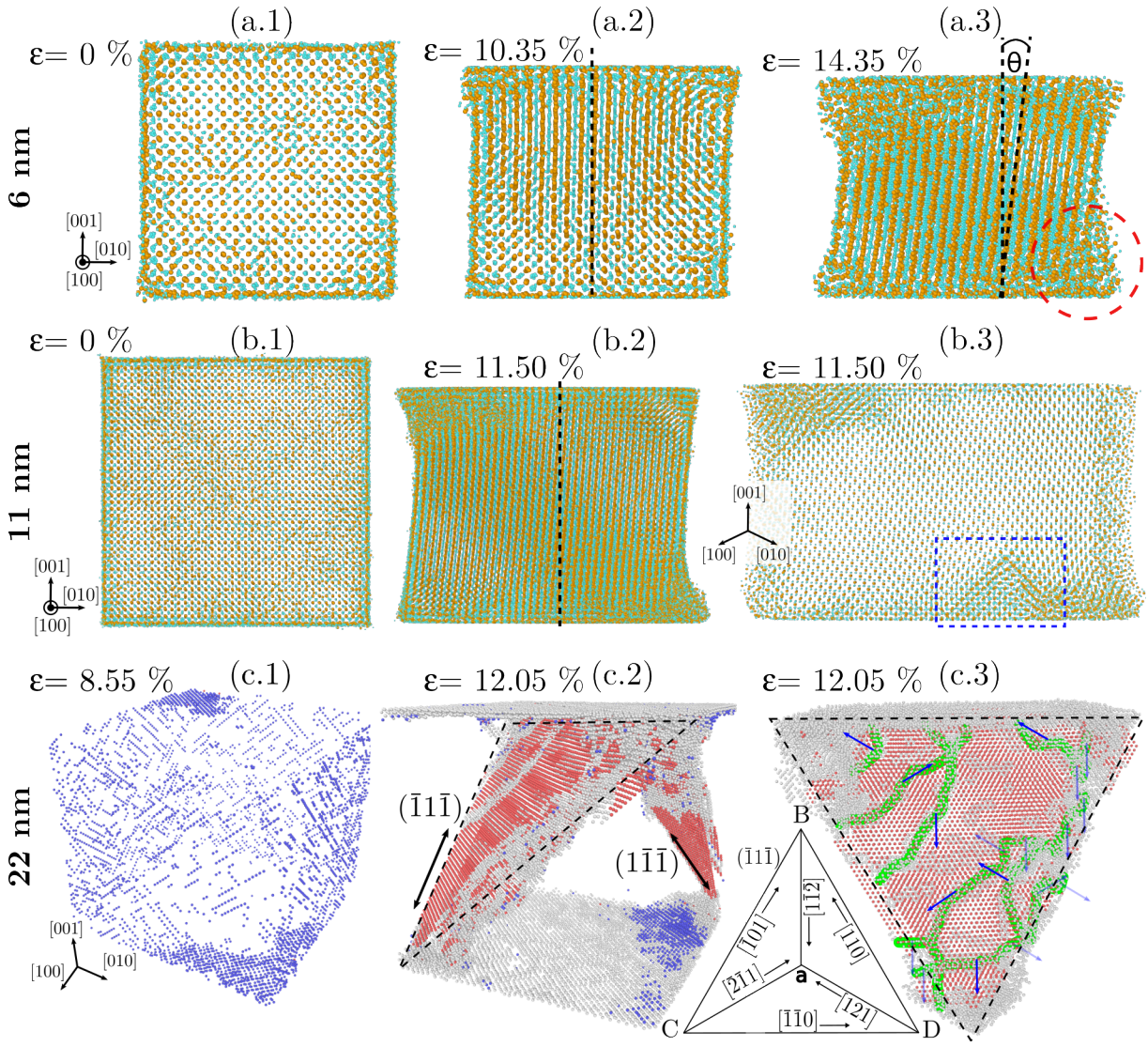

Figure 2: Plastic deformation processes in ceria nanocubes under compression as a function of size. (a) 6, (b) 11, and (c) 22-nm edge size nanocubes. Various deformation processes are illustrated as a function of size including amorphization and reorientation (a.2, a.3, b.2), recrystallization (b.3, c.1), and dislocation and nanotwin formations (c.2, c3). Vertical black dashed lines in (a.2, a.3, b.2) show the compression axis (z-axis), and the oblique black dashed line in (a.3) is the projection of the [001] direction in the drawing plane. In (a.3) the region inside the red dashed circle highlights an extruded amorphous bead at the corner of the sample. The recrystallized phase is detected in (b.3) by the triangular-shape inside the blue dashed rectangle at the bottom of the cube, and by the blue regions of BCC-like symmetry of Ce atoms in (c.1) and (c.2). In (c.2), the $(\bar{1}1\bar{1})$ nanotwin is analyzed in (c.3) using the dislocation analysis (DXA) algorithm, where dislocation fronts of the nanotwin steps are represented by the green lines, and the Burgers vector directions are indicated by the blue arrows. The Thompson tetrahedron shows these directions. Ce and O atoms are respectively colored in orange and turquoise in (a) and (b), while only Ce atoms are displayed in (c) according to their local symmetry, *i.e.* blue, red, and white atoms correspond to bcc, hcp, and no symmetry, respectively.

atomic potential to reproduce elementary atomic processes involved during transformation by a direct comparison to DFT. These results confirm that the recrystallization process observed in CeO_2 is not an artefact due to the Sayle's potential.

In the 11-nm cube, recrystallized regions develop preferentially from the bottom contacting surface and shrink as they progress inside the nanoparticle as shown by the triangular domain obtained in

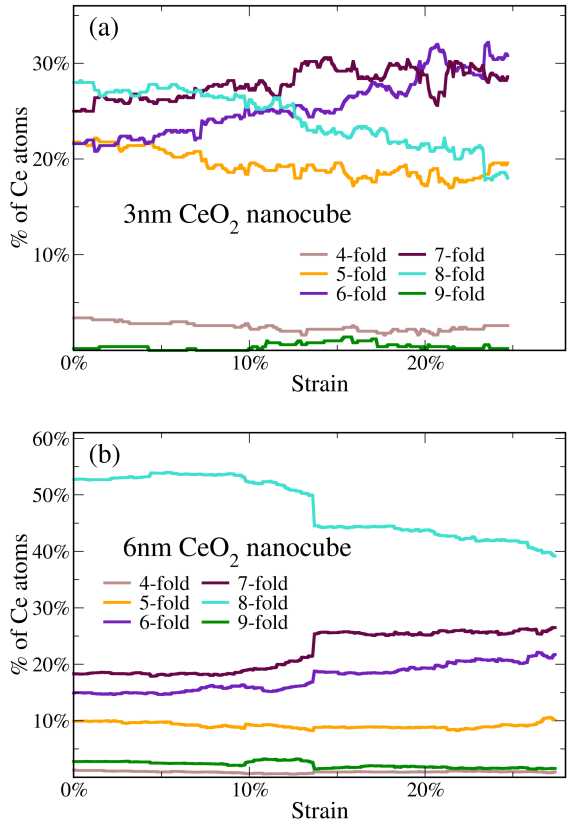

Figure 3: Evolution of the population of Ce atoms with coordination numbers from 4 to 9 as a function of the compressive strain, (a) 3nm nanocube and (b) 6nm nanocube. Ce atoms with coordination numbers out of the [4-9] range represent less than 1% of the total population and are not shown. A cut-off radius of 3Å has been used to define a Ce-O bond.

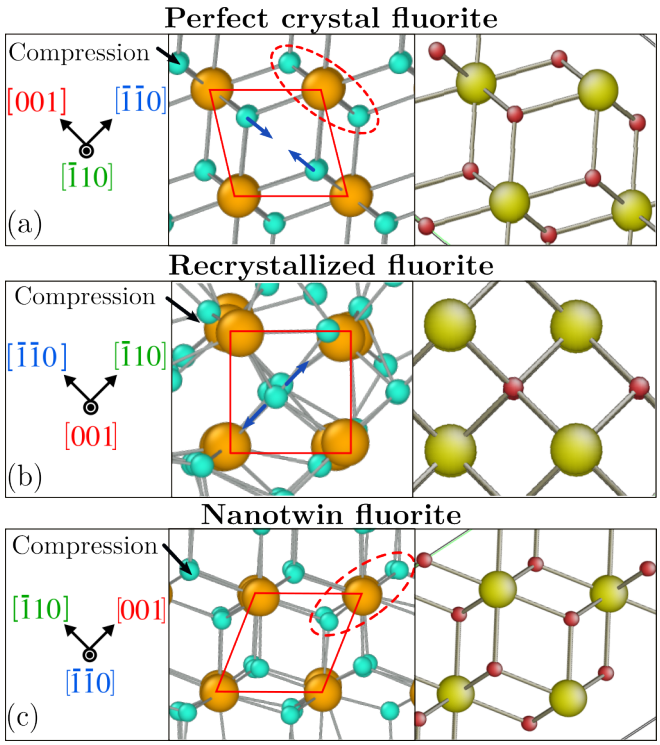

Figure 4: Successive atomic rearrangements during plasticity processes in nanoceria (a) the perfect fluorite structure, (b) recrystallization into a reoriented fluorite structure (c) twinned fluorite structure. Each fluorite structure observed within the compression simulation (middle panel) has been retrieved by orienting an ideal model of the fluorite structure (right panel) according to the directions indicated in the left panel. Ce and O atoms are respectively colored in orange and turquoise in the middle panel, and in yellow and red in the right panel. The compression axis is represented by the black arrow.

Figure 2(b.3) after a projection in the (100) plane. Since recrystallization increases lattice spacing in the original <110> directions, it favors the extrusion of atoms along the same directions close to the indents. Consequently, we observe the development of a tilt angle θ between the compression axis and the original [001] crystallographic direction, as already observed in sub-10 nm size samples. Both of these effects are spotted in Figure 2(b.2).

Thus, the same kind of structural and shape changes as those observed in smaller cubes are observed here but triggered this time by a recrystallization process (intermediate size nanocubes) rather than by amorphization (sub-10 nm size nanocubes). Furthermore, two additional plastic relaxation mechanisms associated to the recrystallization process can be identified in intermediate size samples. First, plastic strain is produced along the compression direction where the [001] direction of the original fluorite structure changes into [110] after recrystallization. Here, the lattice spacing changes from 5.423 Å to 3.835 Å what corresponds to a diminution of about ∼30%. Second, stress dissipation also arises from the reduction of the Young's modulus in the recrystallized zone when switching from the hard [001] direction to the softer [110] (see Young's moduli in table 1). Using local atomic stress field and Voronoi's volumes averaged over ∼300 atoms inside the transformed region, we estimate a stress relaxation of about $\Delta\sigma_{zz}$=-22 GPa between ε=10.05% and ε=12.05% inside the recrystallized domain. This variation is roughly a factor 3 larger than the true stress relaxation in the same strain interval what confirms recrystallization as a

major dissipation process in nanoceria. The definition of the recrystallized region boundaries is not straightforward due to near surface and corners disordering. However, {111} GBs can be identified with respect to the pristine fluorite crystal structure. As the deformation proceeds, already recrystallized domains continue to grow while new recrystallized embryos nucleate close the the top and bottom surfaces of the nanocube.

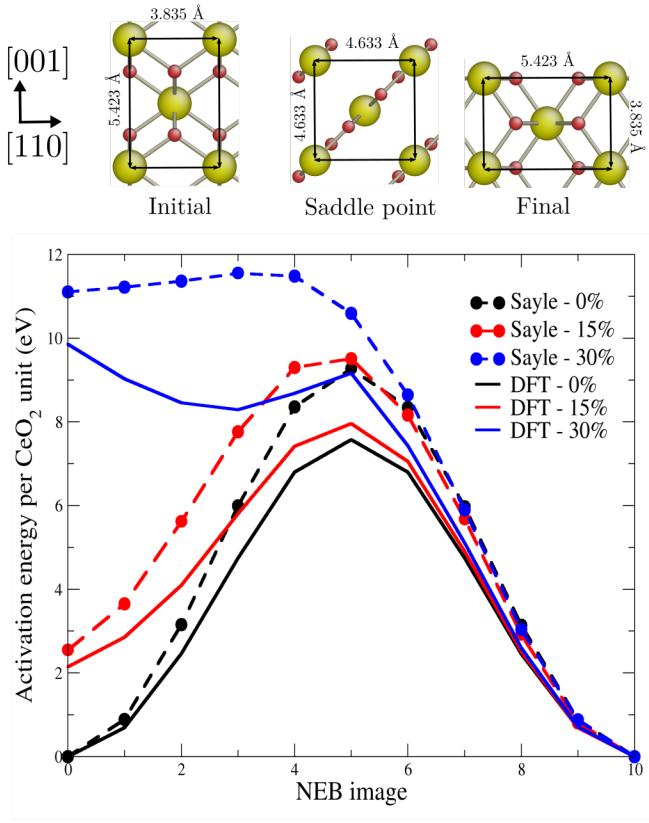

Figure 5: Activation energy for ceria recrystallization (Bain transformation) computed using DFT (full line) and Sayle's potential (dashed line) NEB. The starting NEB configuration is either unconstrained (black) or pre-strained at 15 % (red) or 30 % (blue) strain while the final (recrystallized) configuration is maintained unconstrained. The unit cells of initial, saddle point and final NEB configurations at 0% strain are shown on the top panel.

3.2.3. Larger size nanocubes: 16 and 22 nm

Up to ε ∼12%, all the deformation mechanisms described previously operate in larger nanocubes. While amorphization and disorientation are observed to a lesser extent, the recrystallization process is easily recognized as shown in the 22-nm ceria nanocube (Figure 2(c.1)). Note that because the former FCC cerium sublattice in the recrystallization domain is widely strained, cerium atoms are labelled as BCC by OVITO. This feature also confirms the evolution of the recrystallized Ce network in terms of Bain transformation. Recrystallization-induced plastic relaxation is identified on the stress-strain curve by the first stress diminution at ε=8.5% and in the consecutive strain-hardening regime (up to ε=12.5%) where the recrystallized phase spreads over the surfaces in contact with the indenter and substrate before the occurrence of a massive load drop. The stress dissipation mechanism associated with this catastrophic load drop in larger nanocubes relies on the nucleation of 1/6<112>{111} partial dislocations that quickly evolve into {111} nanotwins that propagate through the nanoparticle. Locally, the nanotwin process initiates from the aformentioned recrystallized domain. Indeed, when Ce layers slip along {111} during the crystal reorientation, an additional slip event leads to the formation of a twinned structure characterized by the well-known mirror symmetry with respect to the perfect crystal structure. One can note that Ce-O bonds in this structural transition tend to align perpendicularly to the compressive axis to reduce the local stress (see Figure 4(c)). Figure 4 shows that the nanotwin process can operate requiring the recrystallized fluorite as an intermediate step between the perfect fluorite crystal and the symmetrically twinned structure. This behaviour is confirmed in Figure 6 where the formation of a nanotwin during the quasi-static compression of 22nm size nanocube is illustrated. In this case, dislocation nucleation occurs at the GB between the strained perfect crystal and a recrystallized domain, GBs (and more commonly defects) being known to behave as sources for the dislocation nucleation process at small-scale [60, 61, 62]. Consistently, we observe that the nanotwin expands preferentially towards neighbouring recrystallized regions, already in the intermediate structure thus facilitating the twin formation. Interestingly, as visible on the left part of Figure 6(c), local and transient recrystallized structures always compose the nanotwin front region.

In all cases, partial dislocations (Figure 6(b)) and nanotwins (Figure 2(c.2) and (c.3)) have 1/6<112> Burgers vectors and {111} slip plane. Few information exists about ceria slip systems and {111} slip planes typical of FCC metals are not particularly expected in spite of their large maximum Schmid factor (∼ 0.47) when compressed along

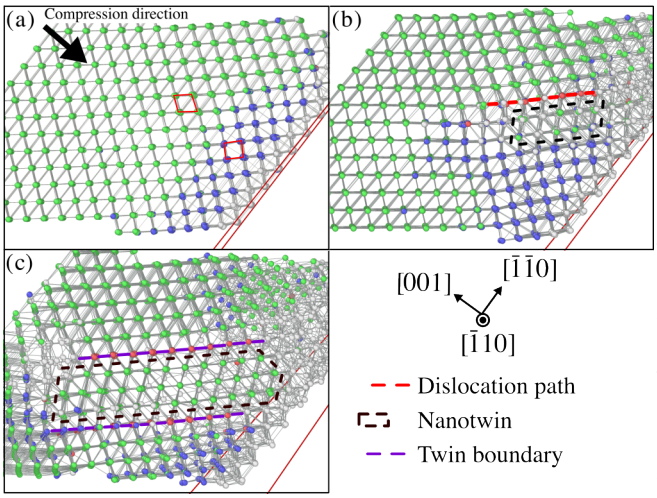

Figure 6: From recrystallization to nanotwin nucleation in ceria nanocube (16 nm edge size, ε=15.7%). (a) Perfect crystal (green atoms) and a thin recrystallized region (blue atoms) near the bottom surface. Local structures characteristic of the perfect crystal (right-oriented Ce parallelogram) and recrystallized phase (square) are highlighted in red. (b) Disorganized and recrystallized regions are produced while a partial dislocation nucleates at the GB (right oriented Ce parallelogram inside the twin boundaries). (c) The nanotwin propagates in the crystal with a twin near-front characterized by a recrystallized structure.

⟨100⟩ [63, 64]. To better assess the nucleation of 1/6<112>{111} partial dislocations in ceria ⟨100⟩ nanoparticles under compression, we perform GSF calculations in several slip planes including {001}, {110}, and {111} under compression perpendicular to the SF plane. On the one hand, ⟨112⟩{111} γ-lines have a double camel humps shape where first maximum and minimum refer to unstable and stable SFE, respectively (see Figure 7(a)). Both properties when computed along ⟨112⟩{111} are commonly used to model dislocation or twin nucleation in FCC metals [44, 45, 65]. On the other hand, ⟨110⟩{100} and ⟨110⟩{110} γ-lines are rather typical of cubic ceramics (not shown). They have a single-hump shape without stable SFE that usually emphasizes the perfect character of 1/2⟨110⟩ dislocations in cubic oxides. For single-hump SFE curves, the unstable SFE is often used to argue on dislocation nucleation, core properties or mobility [50, 66, 67]. For the sake of simplicity, we compare here several unstable SFE in the {100}, {110} and {111} planes, as a function of an imposed compressive strain (see Figure 7(b)). At low strain (ε<10%), the {001} slip plane has the lowest SFE. However, $\frac{1}{2}$⟨110⟩{100} slip systems are characterized by null Schmid factors when compressing along ⟨100⟩ what makes them particularly unfavourable here. Then, up to 30% strain, SFs in the {111} plane are energetically more favorable compared to {100} and {110}, especially when considering ⟨112⟩ directions. Indeed, the ⟨112⟩{111} γ-line is particularly sensitive to the applied strain. Below 15%, the ⟨112⟩{111} γ-lines show a double-camel hump curve with two maxima with comparable orders of magnitude. This kind of γ-line is often observed in oxides (see *e.g.,* Ref. [68]) but very different to the asymetrical curve computed in FCC metals [69]. However, the ⟨112⟩{111} γ-line changes shape when increasing strain further to rather look like the FCC metal ⟨112⟩{111} γ-line *i.e.,* the deformation has an unexpected effect on the SFE in {111} ceria: the effect of ionic charges repulsion on the GSF is reduced by an additional relaxation of oxygen atoms at the in interface (see insets in Figure 7). This makes the 1/6⟨112⟩{111}, FCC-like, stacking-fault more favorable when compared to other stacking-faults in {110} or {100}. Consequently, a new SFE minimum appears at 2.205 Å matching the 1/6<112> *partial* Burgers vector of the {111} slip plane ($b_{1/6<112>}$ = 2.214 Å). When this shift is performed on two parallel and adjacent {111} planes, the local atomic configuration coincides with the nanotwin structure observed during nanocube compression simulations where CeO_2 units are symmetrically tilted out of the original fluorite structure (see structures displayed in Figure 7(a)). Therefore, we believe that {111} twinning associated to local recrystallization might be the main plastic deformation mechanism in pristine nanoscale ceria. One can note that at lower compressive strain, the 1/2⟨110⟩{111} slip system is energetically favourable. This should promote the nucleation of perfect dislocation, especially when nucleation at low strain is possible as in experimental conditions of deformation where the sample may already contain defects.

4. Discussion

4.1. Size effect

Quasi-static atomistic simulations show that plastic deformation mechanisms in ceria nanoparticles depend on size. For small and intermediate sizes, plasticity is dominated by amorphization and/or recrystallization processes which initiate from the surfaces of the cube. The efficiency

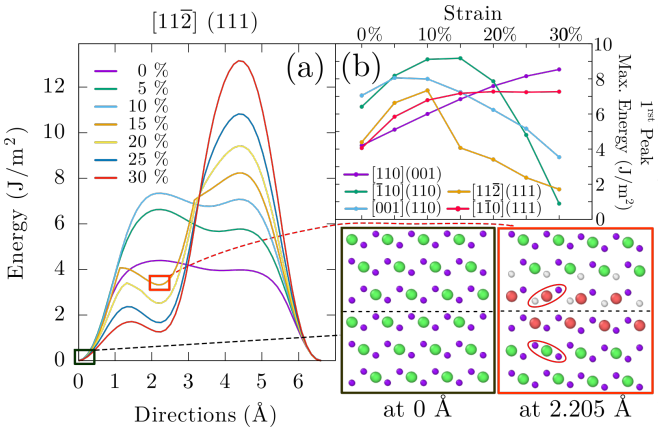

Figure 7: Generalized stacking fault energy profiles as function of strain and slip system. (a) γ-line computed along [11$\bar{2}$] in the (111) slip plane as function of strain (form 0 to 30 %). Insets show the relaxed local atomic configuration computed at displacement 0 and 2.205 Å(15-% GSF curve), respectively. The ceria sublattice is characterized here using the polyhedral template matching algorithm of OVITO. Atoms colored in green, red, purple and light-grey refered to atoms in defective location (FCC, HCP, simple cubic, and no symmetry environment, respectively). (b) Values of the first peak maximum (unstable SFE) of all the computed energy profiles, *i.e.* GSFs on (001), (110), and (111) along coherent slipping directions, with respect to applied strain.

of these dissipation mechanisms are therefore determined by the surface/volume ratio: in small nanocube, this ratio is large and transformation near the surface region provides a significant contribution to the overall stress reduction. The imposed strain can therefore be accommodated by amorphization and/or recrystallization while the stress remains bounded to relatively small values. When increasing the size of the cube, the surface/volume ratio decreases together with the stress dissipation efficiency induced by amorphization and/or recrystallization. This increases the maximum stress with the size of the cube while the system will explore new regions of the potential energy surface, giving access to other dissipation mechanisms. This is what is observed in our larger size nanocubes where surface amorphization and recrystallization both appear but do not account for the largest stress drops. These are due to bulk-like plasticity involving partial dislocations and twins formation. The size dependence of the main plastic deformation mechanism of nanoceria confirms how important it was here to model larger sizes than what is generally done with atomistic simulation of oxides. The largest system sizes investigated in this work are found within the range of ceria nanoparticles usually designed experimentally (from few to hundreds of nm) [53, 70, 71, 72]. However, the 22-nm size remains smalller than the typical dimension ($\sim$ hundred nm) of nanoparticles that are mechanically tested and observed under electronic microscopes [50, 73, 74, 75].

4.2. Comparison with plasticity in FCC metals

The plastic mechanisms involved during the compression of ceria nanocubes can be described as the rearrangements of two atomic sublattices: (i) the Ce sublattice that tends to deform in a rather progressive and continuous manner starting from an FCC structure, (ii) the rearrangement of the oxygen atoms which is more erratic and contributes to the irreversible aspects of the transformations. Focusing on the Ce sublattice, the recrystallization process can be compared to a Bain transformation from a FCC to BCC, as observed in metals. In both cases, the transformation is characterized by the progressive evolution of the cell parameters driven by an external stress. In metallic nanowires, the Bain transformation can be caused solely by the surface stress in absence of other mechanical load [76, 77, 78].

Another similarity with FCC metals is the presence of 1/6<112>{111} partial dislocation in our simulations. In FCC systems, a leading partial dislocation along a 1/6<112> Burgers vector results in an intrinsic stacking fault (ISF) from which three paths are possible: (i) A second trailing partial dislocation with a complementary 1/6<112> Burgers vector nucleates in the same slip plane, both shaping a perfect (or full) dislocation with a Burgers vector of 1/2<110>. Alternatively, successive leading partial dislocations arise on parallel slip planes, they can be (ii) located on non-adjacent planes, slip is thus driven by partial dislocations, or (iii) located in an adjacent slip planes, thus generating nanotwins. This completes the similarities between FCC metals and our simulations of ceria nanocubes where the same twin formation represents the main plastic mechanism for sizes in the 20 nm range.

4.3. Comparison with other systems

At small and intermediate sizes our results on ceria nanocubes under compression show plastic deformations corresponding to amorphization and recystallization which are local phase transformations

driven by the compressive stress. Such kind of plastic transformations are commonly met in mechanical tests of nanosized systems [27, 79]. On the one hand, Raman spectroscopy performed on Y_2O_3 [80] and TiO_2 [81] particles under pressure suggests that amorphization takes place at very small size ($\lesssim$ 10 nm) and crucially depends on the surface treatment of the nanoparticle. These experiments are in line with our simulations where amorphization occurs at the smaller sizes and is probably favoured by the disordered structure of the initial surfaces. Moreover, other MD studies also report amorphization in TiO_2 [82] and CeO_2 [28] nanoparticles. On the other hand, phase transformation in ceria has been reported in the literature both under tension and compression [29, 31]. Sayle *et al.* simulated nanorod deformed along [110] where the relaxation process is driven by a reversible fluorite-to-rutile transition. Another tetragonal phase transition was identified by Park *et al.* as a result of the compression of a thin film [32]. This tetragonal phase was found to be consistent with STEM imaging after compression experiments. In the present work, we evidence a recrystallized phase characterized by the fluorite structure where the hard [001] direction switches from the compression axis to a perpendicular plane while a softer [110]-like crystallographic direction aligns with the compression axis. All these works report different final phases for various systems and dimensions: nanorods under traction, thin films, and nanocubes under compression. However, common features can be highlighted: (i) the CeO bonds tend to rearrange along the plane/direction perpendicular to the effective compression axis (Figure 5 of Ref. [31], Figure 4 of Ref. [32]); (ii) all the structures (both initial and final) can be described by a slight and continuous variation of the Ce atoms while the main difference between them lies in the arrangement of the oxygen sublattice.

In the work of the Sayle's group, only few dislocations were detected such as screw-type dislocations in a simulated crystallized mesoporous structure [34], in a compressed 8-nm nanocube [28], as well as $\langle 110 \rangle \{100\}$ dislocations in compressed nanorods oriented along [110] and [211] [29]. A first explanation for the low amount of dislocations reported in these works comes from the small sizes investigated ($\lesssim$10 nm). Moreover, the preparation of the initial systems relies on the crystallization from liquid particles using MD quenches. As a consequence, their initial structures incorporate many structural defects and deform more easily than our nearly defect-free nanocubes. For instance, the 8-nm nanocube built and compressed in Ref. [28] reaches a yield stress of 12 GPa, against 22 GPa for our 6-nm nanocube. These various simulation conditions make those studies particularly complementary.

5. Conclusion

Defect-free CeO_2 nanocubes with size ranging from 3 to 22 nm are compressed under uniaxial strain along [001] using a classical interatomic potential and quasi-static atomistic simulations. The mechanical properties of CeO_2 nanocubes show a size dependence attributed to changes in the plastic deformation processes. Up to 6 nm edge length (small size), amorphization starting from the sample surface supported by slight crystal reorientations ignite rapidly and accommodate the imposed compression. At intermediate size, amorphization occurs in a lesser extent since the formation of recrystallized regions close to the top and bottom planes is preferred as the main plastic mechanism. The recrystallized phase is identified as a fluorite structure where a local reorganization of the Ce-O bonds leads to a reorientation regarding the compressive direction *i.e.,* switching from a hard [001] direction (in the initial structure) to a soft [110] direction after recrystallization. At larger sizes, the predominant plastic mechanism relies on $1/6\langle 112 \rangle \{111\}$ partial dislocations similar to those observed in FCC metals that nucleate from the recrystallized regions and rapidly form nanotwins propagating into the volume.

Our simulations show an increase of the yield stress with the size of the nanocube in agreement with both the variation of the Young's modulus and the dissipation processes (amorphization and recrystallization) that is reduced as the characteristic size of the nanoparticle increases. Interestingly, our findings exhibit similarities with the plasticity of FCC metals which share the same structure as the Cerium sublattice in ceria. Beyond the characterization of original plastic mechanisms and setting a major benchmark to interpret further experimental and theoretical works about ceria nano-object mechanical properties, our simulations results could help to better understand nanoceria functional properties such as catalysis that is known to be intrinsically related to material defects [83].

6. Declaration of Competing Interest

The authors declare that they have no known competing financial interests or personal relationships that could have appeared to influence the work reported in this paper.

7. Aknowledgments

T. Albaret & G. Laurens aknowledge funding from the ANR MACAO (French Grant No. ANR-18-CE42-0009) and computational resources from the Jean-Zay machine at the Grand Équipement National de Calcul Intensif (GENCI) (Grant No. A0110810637).

References

[1] T. Montini, M. Melchionna, M. Monai, P. Fornasiero, Fundamentals and catalytic applications of ceo2-based materials, Chemical Reviews 116 (10) (2016) 5987–6041. arXiv:https://doi.org/10.1021/acs.chemrev.5b00603, doi:10.1021/acs.chemrev.5b00603.

[2] S. Seal, A. Jeyaranjan, C. J. Neal, U. Kumar, T. S. Sakthivel, D. C. Sayle, Engineered defects in cerium oxides: tuning chemical reactivity for biomedical, environmental, & energy applications, Nanoscale 12 (2020) 6879–6899. doi:10.1039/D0NR01203C.

[3] E. Aneggi, C. de Leitenburg, M. Boaro, P. Fornasiero, A. Trovarelli, 3 - catalytic applications of cerium dioxide, in: S. Scirè, L. Palmisano (Eds.), Cerium Oxide (CeO_2): Synthesis, Properties and Applications, Metal Oxides, Elsevier, 2020, pp. 45–108. doi:https://doi.org/10.1016/B978-0-12-815661-2.00003-7.

[4] B. Li, T. Gu, T. Ming, J. Wang, P. Wang, J. Wang, J. C. Yu, (gold core)@(ceria shell) nanostructures for plasmon-enhanced catalytic reactions under visible light, ACS Nano 8 (8) (2014) 8152–8162. arXiv:https://doi.org/10.1021/nn502303h, doi:10.1021/nn502303h.

[5] A. Diwell, R. Rajaram, H. Shaw, T. Truex, The role of ceria in three-way catalysts, Vol. 71 of Studies in Surface Science and Catalysis, Elsevier, 1991, pp. 139–152. doi:https://doi.org/10.1016/S0167-2991(08)62975-4.

[6] E. Demir, S. Akbayrak, A. M. Önal, S. Özkar, Nanoceria-supported ruthenium(0) nanoparticles: Highly active and stable catalysts for hydrogen evolution from water, ACS Applied Materials & Interfaces 10 (7) (2018) 6299–6308. arXiv:https://doi.org/10.1021/acsami.7b17469, doi:10.1021/acsami.7b17469.

[7] A. Jeyaranjan, T. S. Sakthivel, M. Molinari, D. C. Sayle, S. Seal, Morphology and crystal planes effects on supercapacitance of ceo2 nanostructures: Electrochemical and molecular dynamics studies, Particle & Particle Systems Characterization 35 (10) (2018) 1800176. doi:https://doi.org/10.1002/ppsc.201800176.

[8] Z. Han, F. Kong, X. He, S. Tao, X. Jiang, B. Qian, Ceo_2 nanoparticles embedded into one dimensional n doped carbon matrix as a high performance anode for lithium ion batteries, Journal of Physics and Chemistry of Solids 134 (2019) 187–192. doi:https://doi.org/10.1016/j.jpcs.2019.06.003.

[9] R. Raza, B. Zhu, A. Rafique, M. R. Naqvi, P. Lund, Functional ceria-based nanocomposites for advanced low-temperature (300–600 °c) solid oxide fuel cell: A comprehensive review, Materials Today Energy 15 (2020) 100373. doi:https://doi.org/10.1016/j.mtener.2019.100373.

[10] S. A. Sayyed, N. I. Beedri, P. K. Bhujbal, S. F. Shaikh, H. M. Pathan, Eosin-y sensitized bi-layered zno nanoflower-ceo2 photoanode for dye-sensitized solar cells application, ES Materials & Manufacturing 10 (2020) 45–51. doi:10.30919/esmm5f939.

[11] A. B. Shcherbakov, N. M. Zholobak, V. K. Ivanov, 8 - biological, biomedical and pharmaceutical applications of cerium oxide, in: S. Scirè, L. Palmisano (Eds.), Cerium Oxide (CeO_2): Synthesis, Properties and Applications, Metal Oxides, Elsevier, 2020, pp. 279–358. doi:https://doi.org/10.1016/B978-0-12-815661-2.00008-6.

[12] T. Pirmohamed, J. M. Dowding, S. Singh, B. Wasserman, E. Heckert, A. S. Karakoti, J. E. S. King, S. Seal, W. T. Self, Nanoceria exhibit redox state-dependent catalase mimetic activity, Chem. Commun. 46 (2010) 2736–2738. doi:10.1039/B922024K.

[13] A. B. Shcherbakov, N. M. Zholobak, N. Y. Spivak, V. K. Ivanov, Advances and prospects of using nanocrystalline ceria in cancer theranostics, Russian Journal of Inorganic Chemistry 59 (2014) 1556–1575. doi:10.1134/S003602361413004X.

[14] S. Naz, J. Beach, B. Heckert, T. Tummala, O. Pashchenko, T. Banerjee, S. Santra, Cerium oxide nanoparticles: a 'radical' approach to neurodegenerative disease treatment, Nanomedicine 12 (5) (2017) 545–553. arXiv:https://doi.org/10.2217/nnm-2016-0399, doi:10.2217/nnm-2016-0399.

[15] T. X. T. Sayle, S. C. Parker, D. C. Sayle, Oxidising co to co2 using ceria nanoparticles, Phys. Chem. Chem. Phys. 7 (2005) 2936–2941. doi:10.1039/B506359K.

[16] T. Sayle, S. Parker, C. Catlow, The role of oxygen vacancies on ceria surfaces in the oxidation of carbon monoxide, Surface Science 316 (3) (1994) 329–336. doi:https://doi.org/10.1016/0039-6028(94)91225-4.

[17] N. V. Skorodumova, M. Baudin, K. Hermansson, Surface properties of ceo_2 from first principles, Phys. Rev. B 69 (2004) 075401. doi:10.1103/PhysRevB.69.075401.

[18] M. Lundberg, B. Skårman, L. Reine Wallenberg, Crystallography and porosity effects of co conversion on mesoporous ceo2, Microporous and Mesoporous Materials 69 (3) (2004) 187–195. doi:https://doi.org/10.1016/j.micromeso.2004.02.009.

[19] K. Zhou, X. Wang, X. Sun, Q. Peng, Y. Li, Enhanced catalytic activity of ceria nanorods from well-defined reactive crystal planes, Journal of Catalysis 229 (1) (2005) 206–212. doi:https://doi.org/10.1016/j.jcat.2004.11.004.

[20] N. J. Lawrence, J. R. Brewer, L. Wang, T.-S. Wu, J. Wells-Kingsbury, M. M. Ihrig, G. Wang, Y.-L. Soo, W.-N. Mei, C. L. Cheung, Defect engineering in cubic cerium oxide nanostructures for catalytic oxidation, Nano Letters 11 (7) (2011)

2666–2671. arXiv:https://doi.org/10.1021/nl200722z, doi:10.1021/nl200722z.

[21] M. V. Landau, R. Vidruk, D. Vingurt, D. Fuks, M. Herskowitz, Grain boundaries in nanocrystalline catalytic materials as a source of surface chemical functionality, Reviews in Chemical Engineering 30 (4) (2014) 379–401. doi:doi:10.1515/revce-2014-0011.

[22] J. An, J. Bae, S. Hong, B. Koo, Y.-B. Kim, T. M. Gür, F. B. Prinz, Grain boundary blocking of ionic conductivity in nanocrystalline yttria-doped ceria thin films, Scripta Materialia 104 (2015) 45–48. doi:https://doi.org/10.1016/j.scriptamat.2015.03.020.

[23] A. R. Symington, M. Molinari, J. Statham, J. Wu, S. C. Parker, The role of dopant segregation on the oxygen vacancy distribution and oxygen diffusion in CeO2 grain boundaries, Journal of Physics: Energy 1 (4) (2019) 042005. doi:10.1088/2515-7655/ab28b5.

[24] M. D. Uchic, D. M. Dimiduk, J. N. Florando, W. D. Nix, Sample dimensions influence strength and crystal plasticity, Science 305 (5686) (2004) 986–989.

[25] J. R. Greer, J. T. M. De Hosson, Plasticity in small-sized metallic systems: Intrinsic versus extrinsic size effect, Progress in Materials Science 56 (6) (2011) 654–724.

[26] D. Mordehai, O. David, R. Kositski, Nucleation-controlled plasticity of metallic nanowires and nanoparticles, Advanced Materials 30 (41) (2018) 1706710.

[27] J. Amodeo, L. Pizzagalli, Modeling the mechanical properties of nanoparticles: a review, Comptes Rendus Physique 22 (3) (2021) 35–66. doi:0.5802/crphys.70.

[28] F. Caddeo, A. Corrias, D. C. Sayle, Tuning the properties of nanoceria by applying force: Stress-induced ostwald ripening, The Journal of Physical Chemistry C 120 (26) (2016) 14337–14344. arXiv:https://doi.org/10.1021/acs.jpcc.6b02279, doi:10.1021/acs.jpcc.6b02279.

[29] T. X. T. Sayle, B. J. Inkson, A. Karakoti, A. Kumar, M. Molinari, G. Möbus, S. C. Parker, S. Seal, D. C. Sayle, Mechanical properties of ceria nanorods and nanochains; the effect of dislocations, grain-boundaries and oriented attachment, Nanoscale 3 (2011) 1823–1837. doi:10.1039/C0NR00980F.

[30] L. M. Morgan, M. Molinari, A. Corrias, D. C. Sayle, Protecting ceria nanocatalysts—the role of sacrificial barriers, ACS Applied Materials & Interfaces 10 (38) (2018) 32510–32515. arXiv:https://doi.org/10.1021/acsami.8b08674, doi:10.1021/acsami.8b08674.

[31] T. X. T. Sayle, D. C. Sayle, Elastic deformation in ceria nanorods via a fluorite-to-rutile phase transition, ACS Nano 4 (2) (2010) 879–886. arXiv:https://doi.org/10.1021/nn901612s, doi:10.1021/nn901612s.

[32] K.-W. Park, C. S. Kim, Deformation-induced charge redistribution in ceria thin film at room temperature, Acta Materialia 191 (2020) 70–80. doi:https://doi.org/10.1016/j.actamat.2020.03.029.

[33] A. P. Thompson, H. M. Aktulga, R. Berger, D. S. Bolintineanu, W. M. Brown, P. S. Crozier, P. J. in't Veld, A. Kohlmeyer, S. G. Moore, T. D. Nguyen, R. Shan, M. J. Stevens, J. Tranchida, C. Trott, S. J. Plimpton, LAMMPS - a flexible simulation tool for particle-based materials modeling at the atomic, meso, and continuum scales, Computer Physics Communications 271 (2022) 108171. doi:10.1016/j.cpc.2021.108171.

[34] T. X. T. Sayle, M. Cantoni, U. M. Bhatta, S. C. Parker, S. R. Hall, G. Möbus, M. Molinari, D. Reid, S. Seal, D. C. Sayle, Strain and architecture-tuned reactivity in ceria nanostructures; enhanced catalytic oxidation of co to co2, Chemistry of Materials 24 (10) (2012) 1811–1821. arXiv:https://doi.org/10.1021/cm3003436, doi:10.1021/cm3003436.

[35] D. J. Hardy, J. E. Stone, K. Schulten, Multilevel summation of electrostatic potentials using graphics processing units, Parallel computing 35 (3) (2009) 164–177.

[36] E. Bitzek, P. Koskinen, F. Gähler, M. Moseler, P. Gumbsch, Structural relaxation made simple, Phys. Rev. Lett. 97 (2006) 170201. doi:10.1103/PhysRevLett.97.170201.

[37] G. Kresse, J. Furthmüller, Efficient iterative schemes for ab initio total-energy calculations using a plane-wave basis set, Phys. Rev. B 54 (1996) 11169. doi:10.1103/PhysRevB.54.11169.

[38] G. Kresse, D. Joubert, From ultrasoft pseudopotentials to the projector augmented waves method, Phys. Rev. B 59 (1999) 1758. doi:10.1103/PhysRevB.59.1758.

[39] P. E. Blöchl, Projector augmented-wave method, Phys. Rev. B 50 (1994) 17953. doi:10.1103/PhysRevB.50.17953.

[40] J. P. Perdew, A. Zunger, Self-interaction correction to density-functional approximations for many-electron systems, Physical Review B 23 (10) (1981) 5048.

[41] S. L. Dudarev, G. A. Botton, S. Y. Savrasov, C. J. Humphreys, A. P. Sutton, Electron-energy-loss spectra and the structural stability of nickel oxide: An lsda+u study, Phys. Rev. B 57 (1998) 1505–1509. doi:10.1103/PhysRevB.57.1505.

[42] A. Nakajima, A. Yoshihara, M. Ishigame, Defect-induced raman spectra in doped ceo_2, Phys. Rev. B 50 (1994) 13297–13307. doi:10.1103/PhysRevB.50.13297.

[43] V. Vítek, Intrinsic stacking faults in body-centred cubic crystals, The Philosophical Magazine: A Journal of Theoretical Experimental and Applied Physics 18 (154) (1968) 773–786. arXiv:https://doi.org/10.1080/14786436808227500, doi:10.1080/14786436808227500.

[44] M. Chen, E. Ma, K. J. Hemker, H. Sheng, Y. Wang, X. Cheng, Deformation twinning in nanocrystalline aluminum, Science 300 (5623) (2003) 1275–1277.

[45] H. Van Swygenhoven, P. M. Derlet, A. Frøseth, Stacking fault energies and slip in nanocrystalline metals, Nature Materials 3 (6) (2004) 399–403.

[46] J. Guénolé, S. Brochard, J. Godet, Unexpected slip mechanism induced by the reduced dimensions in silicon nanostructures: Atomistic study, Acta Materialia 59 (20) (2011) 7464–7472. doi:https://doi.org/10.1016/j.actamat.2011.08.039.

[47] P. Tasker, The stability of ionic crystal surfaces, Journal of Physics C: Solid State Physics 12 (22) (1979) 4977.

[48] C. Noguera, Polar oxide surfaces, Journal of Physics: Condensed Matter 12 (31) (2000) R367.

[49] T. Albaret, A. Tanguy, F. Boioli, D. Rodney, Mapping between atomistic simulations and eshelby inclusions in the shear deformation of an amorphous silicon model, Physical Review E 93 (5) (2016) 053002.

[50] I. Issa, J. Amodeo, J. Réthoré, L. Joly-Pottuz, C. Esnouf, J. Morthomas, M. Perez, J. Chevalier, K. Masanelli-Varlot, In situ investigation of mgo nanocube deformation at room temperature, Acta Mater. 86 (2015) 295–304.

doi:10.1016/j.actamat.2014.12.001.
[51] A. Stukowski, Visualization and analysis of atomistic simulation data with OVITO-the Open Visualization Tool, Model. Simul. Mater. Sci. Eng. 18 (1) (JAN 2010). doi:10.1088/0965-0393/18/1/015012.
[52] J. D. Honeycutt, H. C. Andersen, Molecular dynamics study of melting and freezing of small lennard-jones clusters, Journal of Physical Chemistry 91 (19) (1987) 4950–4963.
[53] U. Castanet, C. Feral-Martin, A. Demourgues, R. L. Neale, D. C. Sayle, F. Caddeo, J. M. Flitcroft, R. Caygill, B. J. Pointon, M. Molinari, J. Majimel, Controlling the 111/110 surface ratio of cuboidal ceria nanoparticles, ACS Applied Materials & Interfaces 11 (12) (2019) 11384–11390. arXiv:https://doi.org/10.1021/acsami.8b21667, doi:10.1021/acsami.8b21667.
[54] J. Amodeo, K. Lizoul, Mechanical properties and dislocation nucleation in nanocrystals with blunt edges, Materials and Design 135 (2017-12) 223 – 231. doi:10.1016/j.matdes.2017.09.009.
[55] D. Kilymis, C. Gerard, J. Amodeo, U. V. Waghmare, L. Pizzagalli, Uniaxial compression of silicon nanoparticles: An atomistic study on the shape and size effects, Acta Materialia 158 (2018) 155 – 166. doi:10.1016/j.actamat.2018.07.063.
[56] J. Wortman, R. Evans, Young's modulus, shear modulus, and poisson's ratio in silicon and germanium, Journal of applied physics 36 (1) (1965) 153–156.
[57] E. C. Bain, The nature of martensite, Trans. Am. Inst. Min. Metall. Eng. 70 (1924) 25.
[58] H. Jónsson, G. Mills, K. W. Jacobsen, Nudged elastic band method for finding minimum energy paths of transitions, in: B. J. Berne, G. Ciccotti, D. F. Coker (Eds.), Classical and Quantum Dynamics in Condensed Phase Simulations, World Scientific, Singapore, 1998, p. 385.
[59] G. Henkelman, B. P. Uberuaga, H. Jónsson, A climbing image nudged elastic band method for finding saddle points and minimum energy paths, The Journal of chemical physics 113 (22) (2000) 9901–9904.
[60] H. V. Swygenhoven, P. M. Derlet, A. G. Frøseth, Nucleation and propagation of dislocations in nanocrystalline fcc metals, Acta Materialia 54 (7) (2006-04) 1975 – 1983. doi:10.1016/j.actamat.2005.12.026.
[61] J. Kacher, B. Eftink, B. Cui, I. Robertson, Dislocation interactions with grain boundaries, Current Opinion in Solid State and Materials Science 18 (4) (2014) 227–243. doi:10.1016/j.cossms.2014.05.004.
[62] X. Li, H. Long, J. Zhang, D. Ma, D. Kong, Y. Lu, S. Sun, J. Cai, X. Wang, L. Wang, S. Mao, Direct observation of the grain boundaries acting as dislocation sources in nanocrystalline platinum, Materials Characterization 181 (2021) 111493. doi:10.1016/j.matchar.2021.111493.
[63] A. G. Evans, P. L. Pratt, Dislocations in the fluorite structure, Philosophical Magazine 20 (168) (1969) 1213–1237. doi:10.1080/14786436908228207.
[64] L. Portelette, J. Amodeo, R. Madec, J. Soulacroix, T. Helfer, B. Michel, Crystal viscoplastic modeling of UO2 single crystal, Journal of Nuclear Materials 510 (2018) 635–643. doi:10.1016/j.jnucmat.2018.06.035.
[65] C. R. Weinberger, W. Cai, Plasticity of metal nanowires, J. Mater. Chem. 22 (2012) 3277–3292. doi:10.1039/C2JM13682A.
[66] J. Amodeo, P. Carrez, B. Devincre, P. Cordier, Multiscale modelling of MgO plasticity, Acta Materialia 59 (6) (2011) 2291 – 2301. doi:10.1016/j.actamat.2010.12.020.
[67] R. Skelton, A. M. Walker, Peierls-Nabarro modeling of dislocations in UO2, Journal of Nuclear Materials 495 (2017) 202 – 210. doi:10.1016/j.jnucmat.2017.08.024.
[68] Q. Xu, N. Salles, J. Chevalier, J. Amodeo, Atomistic simulation and interatomic potential comparison in α-Al_2O_3: lattice, surface and extended-defects properties, Modelling and Simulation in Materials Science and Engineering 30 (3) (2022) 035008. doi:10.1088/1361-651x/ac4d76.
[69] J. A. Zimmerman, H. J. Gao, F. F. Abraham, Generalized stacking fault energies for embedded atom FCC metals, Modelling and Simulation in Materials Science and Engineering 8 (2) (2000-03) 103 – 115. doi:10.1088/0965-0393/8/2/302.
[70] M. Bugnet, S. H. Overbury, Z. L. Wu, T. Epicier, Direct visualization and control of atomic mobility at 100 surfaces of ceria in the environmental transmission electron microscope, Nano Lett. 17 (2017) 7652–7658. doi:10.1021/acs.nanolett.7b03680.
[71] I. Trenque, G. C. Magnano, M. A. Bolzinger, L. Roiban, F. Chaput, I. Pitault, S. Briançon, T. Devers, K. Masenelli-Varlot, M. Bugnet, D. Amans, Shape-selective synthesis of nanoceria for degradation of paraoxon as a chemical warfare simulant, Phys. Chem. Chem. Phys. 21 (2019) 5455–5465. doi:10.1039/C9CP00179D.
[72] I. Trenque, G. C. Magnano, J. Bárta, F. Chaput, M. A. Bolzinger, I. Pitault, S. Briançon, K. Masenelli-Varlot, M. Bugnet, C. Dujardin, V. Čuba, D. Amans, Synthesis routes of ceo2 nanoparticles dedicated to organophosphorus degradation: a benchmark, CrystEngComm 22 (2020) 1725–1737. doi:10.1039/C9CE01898K.
[73] J. Deneen, W. M. Mook, A. Minor, W. W. Gerberich, C. Barry Carter, In situ deformation of silicon nanospheres, Journal of materials science 41 (14) (2006) 4477–4483.
[74] C. Carlton, P. Ferreira, In situ tem nanoindentation of nanoparticles, Micron 43 (11) (2012) 1134–1139.
[75] A. Sharma, J. Amodeo, N. Gazit, Y. Qi, O. Thomas, E. Rabkin, When more is less: Plastic weakening of single crystalline ag nanoparticles by the polycrystalline au shell, ACS nano 15 (9) (2021) 14061–14070.
[76] J. Diao, K. Gall, M. L. Dunn, Surface-stress-induced phase transformation in metal nanowires, Nature Materials 2 (2003) 656–660. doi:10.1038/nmat977.
[77] K. Gall, J. Diao, M. L. Dunn, M. Haftel, N. Bernstein, M. J. Mehl, Tetragonal Phase Transformation in Gold Nanowires, Journal of Engineering Materials and Technology 127 (4) (2005) 417–422. doi:10.1115/1.1924558.
[78] M. I. Haftel, K. Gall, Density functional theory investigation of surface-stress-induced phase transformations in fcc metal nanowires, Phys. Rev. B 74 (2006) 035420. doi:10.1103/PhysRevB.74.035420.
[79] D. Machon, V. Pischedda, S. Le Floch, A. San-Miguel, Perspective: High pressure transformations in nanomaterials and opportunities in material design, Journal of Applied Physics 124 (16) (2018) 160902.
[80] L. Piot, S. Le Floch, T. Cornier, S. Daniele, D. Machon, Amorphization in nanoparticles, The Journal of Physical Chemistry C 117 (21) (2013) 11133–11140.
[81] D. Machon, M. Daniel, P. Bouvier, S. Daniele, S. Le Floch, P. Melinon, V. Pischedda, Interface energy

impact on phase transitions: the case of tio2 nanoparticles, The Journal of Physical Chemistry C 115 (45) (2011) 22286–22291.

[82] V. Pischedda, G. Hearne, A. Dawe, J. Lowther, Ultrastability and enhanced stiffness of 6 nm tio 2 nanoanatase and eventual pressure-induced disorder on the nanometer scale, Physical review letters 96 (3) (2006) 035509.

[83] L. Wu, A. J. Van Hoof, N. Y. Dzade, L. Gao, M.-I. Richard, H. Friedrich, N. H. De Leeuw, E. J. Hensen, J. P. Hofmann, Enhancing the electrocatalytic activity of 2h-ws 2 for hydrogen evolution via defect engineering, Physical Chemistry Chemical Physics 21 (11) (2019) 6071–6079.